ChemComm

COMMUNICATION

Cite this: *Chem. Commun.*, 2024, **60**, 3531

Received 5th January 2024,
Accepted 28th February 2024

DOI: 10.1039/d4cc00068d

rsc.li/chemcomm

High photocatalytic performance over ultrathin 2D TiO_2 for CO_2 reduction to alcohols†

Chenxu Yin,[a] Xue Li,[a] Shangcong Sun,[b] Xiaoqian Wei,[a] Qing Tong,[a] Wei Tan,[a] Xin Wang,[a] Bo Peng,*[b] Haiqin Wan *[a] and Lin Dong [a]

We report a noble-metal-free photocatalyst, ultrathin TiO_2 with atomic layer thickness, which is a potential catalyst for CO_2 photoreduction. An excellent liquid-product yield of 463.9 μmol g_{cat}^{-1} in 8 h with 98% selectivity to alcohols was achieved, owing to sufficient surface defects favoring CO_2 adsorption/activation.

Growing interest has been shown in solar-driven conversion of CO_2 and H_2O into high-energy fuels and green chemicals, which presents a viable approach to simultaneously address global warming and the energy crisis.[1,2] Nevertheless, most photocatalysts developed to date favor the generation of gaseous products over more valuable liquid C2 compounds,[3] owing to complicated multi-electron/proton transfer processes and high energy barriers during C–C coupling to generate key *C2 intermediates.[4,5] Therefore, the activation of inert CO_2, stabilization of *CO intermediates, and favorable formation of *C2 intermediates, should be taken into consideration in the rational design of highly efficient photocatalysts for CO_2 reduction to liquid products.

Titanium dioxide (TiO_2) is a classical photocatalyst used extensively, due to its stable physicochemical properties, non-toxicity, low cost, *etc.*[6] However, the poor electron–hole pair separation efficiency greatly restricts the multi-step proton/electron transfer, limiting the formation of liquid products.[7,8] An atomically thin two-dimensional (2D) structure has sparked significant curiosity for CO_2 conversion.[9–11] The regulation of photomaterial thickness is an advantageous approach for producing oxygen vacancies under control, which can likewise enrich the reactive intermediates, resulting in low-coordinated atoms on the catalyst surface, which in turn facilitates the C–C bond formation during CO_2 reduction to liquid products.[12–14] Considering that the ultrathin materials possess not only rich defects, but also large surface areas, we are aiming for ultrathin TiO_2 in this work.

Herein, we present the synthesis of ultrathin TiO_2 nanosheets by a solvothermal method.[15] The resulting ultrathin TiO_2 nanosheets displayed high CO_2 adsorption capacity and activation ability, which was essential to the efficient conversion of CO_2 into liquid products without any co-catalyst.

Our synthetic strategy starts with an ethylene glycol solution of titanium tetrachloride as the precursor, mixed with alcohol/water before a solvo-/hydro-thermal step (see details in the ESI†). During the rapid heating of the hydrous-/oxy-chloride precursors, the precursors were hydrolyzed, causing the spontaneous formation of ultrathin TiO_2 nanosheets under the self-generated pressure.[11] The nanosheets were denoted as UT-M, UT-E, and UT-W, with methanol, ethanol, and distilled water as the added solvents, respectively.

The morphology of the as-synthesized samples was characterized by transmission electron microscopy (TEM). All samples displayed a wrinkle-like structure and the lateral size is 150–200 nm, with randomly stacked nanosheets with the edges rolled up (Fig. 1(a)–(c) and Fig. S1, ESI†). DLS also suggested that the prepared ultrathin TiO_2 was an irregular film or sheet (Fig. S2, ESI†). Atomic force microscopy (AFM) analysis showed that the thickness of UT-E, UT-M and UT-W was averaged to be 0.4, 0.9, and 0.7 nm, respectively (Fig. 1(d)–(g)). The crystalline structure of the samples was determined by X-ray diffraction (XRD) as shown in Fig. 1(h) and Fig. S3 (ESI†). All the samples show similar XRD profiles matching well with the metastable polymorph TiO_2(B) (JCPDS card no. 74-1940; space group: $C2/m$) without other crystalline phases. TiO_2(B) is mainly derived from layered titanate and its octahedral units are arranged in wavy sheets that consist of both edge- and corner-shared TiO_6 octahedra. Interestingly, a new peak appears at 7.5°, which is at smaller 2θ than the lowest-indexed (001) plane and could be ascribed to the interlayer distance of the 2D morphology.[16] The results of Raman spectroscopy of the samples were in good agreement with the above statements (Fig. S4, ESI†). Information on the porous structures has been acquired by N_2 physisorption (Fig. S5 and Table S1, ESI†). Apparently, based on the

[a] *State Key Laboratory of Pollution Control and Resource Reuse, School of the Environment, Centre of Modern Analysis, Jiangsu Key Laboratory of Vehicle Emissions Control, Nanjing University, Nanjing 210023, China. E-mail: wanhq@nju.edu.cn*

[b] *SINOPEC Research Institute of Petroleum Processing Co., Ltd., Beijing 100083, China. E-mail: pengbo.ripp@sinopec.com*

† Electronic supplementary information (ESI) available. See DOI: https://doi.org/10.1039/d4cc00068d

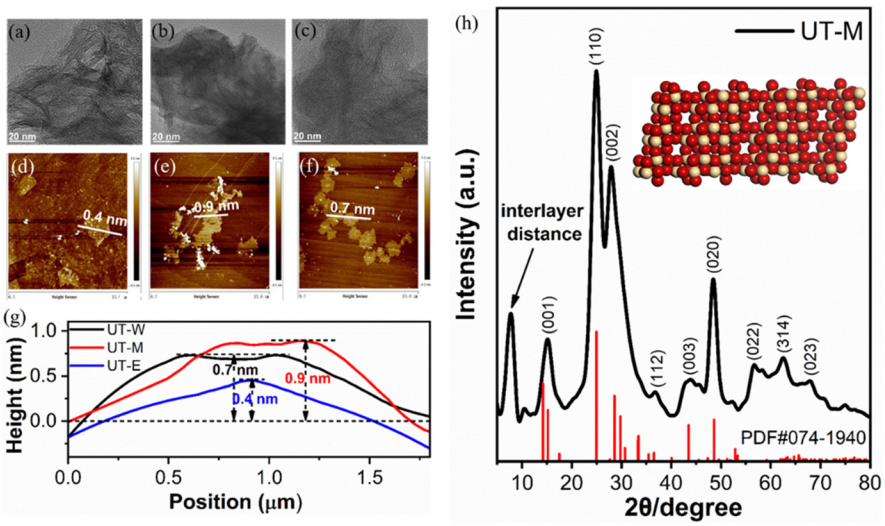

Fig. 1 TEM and AFM images of (a) and (d) UT-E, (b) and (e) UT-M, and (c) and (f) UT-W; (g) AFM height profiles of various catalysts; and (h) XRD of UT-M with the peak positions of standard polymorph TiO_2(B) shown in red lines as a comparison. Inset: TiO_2(B) structure.

above-mentioned characterizations, we have successfully synthesized ultrathin TiO_2 nanosheets with atomic thicknesses.

The photocatalytic CO_2 reduction performance of the as-synthesized materials was tested in the presence of water vapor medium under full-spectrum light irradiation. The liquid products were monitored and analyzed using a GC-FID, as presented in Fig. 2(a) and Fig. S6 (ESI†). The pristine titanium dioxide nanosheets of anatase phase and the commercial P25 (physicochemical properties are available in the ESI†), only produce CO and CH_4 (Fig. S7, ESI†). In comparison, apart from these gaseous products, large quantities of CH_3OH and C_2H_5OH were generated on the ultrathin TiO_2 nanosheets, manifesting the highly active CO_2 photocatalytic reduction performance. Impressively, UT-M exhibits the highest photocatalytic CO_2 conversion efficiency among all the TiO_2 nanosheet catalysts tested, with a yield of 166.2 and 297.7 μmol g_{cat}^{-1} for CH_3OH and C_2H_5OH, respectively. In addition, it also displayed the highest electron-based selectivity of 76.8% towards C_2H_5OH and 98.2% towards all liquid products (Fig. 2(b)), demonstrating its strong capability of C–C coupling. Next, a Xe lamp with different filters, including 365 nm, 420 nm and 450 nm, was also utilized for quantum efficiency trials for UT-M, showing that 365 nm is the optimal light source, giving 8.7% and 18.3% QE for methanol and ethanol, respectively (Table S2, ESI†). The distinctive CO_2 reduction activity and high selectivity towards C_2H_5OH and total liquid products are still well maintained after three-cycle tests of 24 h in total, demonstrating the excellent stability of the catalyst (Fig. S8, ESI†). A series of control experiments were performed in the absence of illumination, the catalyst or CO_2, and no liquid products were detected (Fig. S9, ESI†). It still remains debatable whether the liquid products are from the CO_2 feed, as another carbon source was utilized during the catalyst synthesis. To verify this issue, a $^{13}CO_2$ isotopic labelling experiment and ^{12}C mass spectrometry of standard methanol/ethanol were carried out. The results of ^{13}C GC-MS showed m/z = 32 and 45 signals, while a signal at m/z = 31 peak, which was the strongest peak in ^{12}C methanol and ethanol, was not observed. Combining the long-term experimental results, m/z = 32 and 45 were assigned to $^{13}CH_3O$ and $^{13}CO_2$. Therefore, it is demonstrated that the liquid products originate from the CO_2 feed instead of possible carbon-containing species on the catalyst surface (Fig. 2(c) and Fig. S10, ESI†). Compared to the recent literature results listed in Table S3 (ESI†), the UT-M catalyst is among

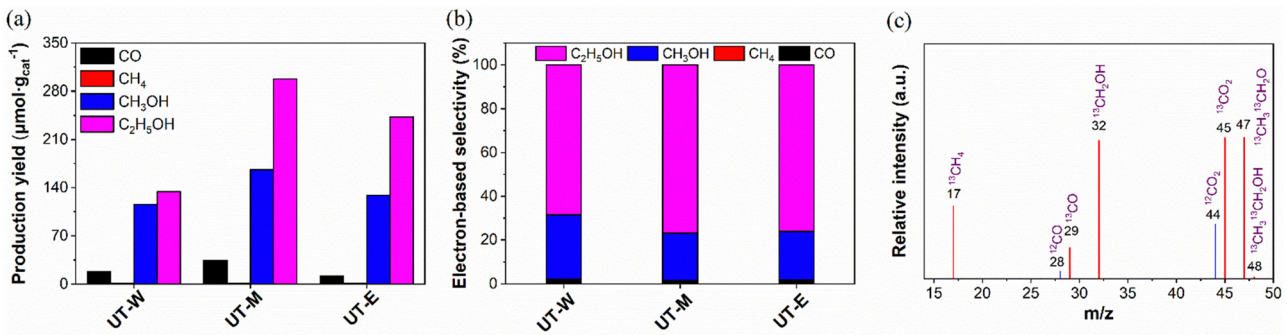

Fig. 2 Photocatalytic CO_2 reduction performance on UT-W, UT-M, and UT-E. (a) Production generation rate. (b) Electron-based selectivity of UT-W, UT-M, and UT-E. (c) GC-MS spectrum of the ^{13}C liquid products from photocatalytic $^{13}CO_2$ reduction on UT-M.

the most active photocatalysts. It is worth mentioning that it has no noble-metal content at all and reacts without any sacrificial agent.

In order to give more insight into the structural origin of the excellent catalytic activity, the charge carrier dynamics and the light utilization were studied. According to the UV-Vis diffuse reflectance spectra (Fig. S11, ESI†), all the catalysts showed strong adsorption peaks between 250 and 400 nm, corresponding to the charge transfer from the valence band (VB) O 2p orbital to the conduction band (CB) Ti 3d orbital. The band gaps of UT-W, UT-M, and UT-E were calculated as 3.60, 3.16, and 3.43 eV, respectively. UT-M is able to migrate more electrons to the CB during reaction, which is beneficial for CO_2 reduction to CH_3OH/C_2H_5OH. Furthermore, the CB potentials of UT-W, UT-M, and UT-E are −2.14, −1.91, and −2.04 eV, respectively (Fig. S12, ESI†). In addition, photoelectrochemical (PEC) analysis showed that UT-M affords the highest photocurrent density, the smallest semicircle in the Nyquist plots, and the weakest photoluminescence (with an excitation of 325 nm) emission peak intensity (Fig. S13 and S14, ESI†), suggesting that the fast charge carrier dynamics of UT-M is kinetically favored for the multi-electron reactions of generating liquid products.

To identify the role of surface defects, the catalysts were investigated by XPS, electron spin resonance (ESR), and water contact angle analysis. The Ti 2p XPS spectra shown in Fig. 3(a) displayed a set of doublets centered at binding energies (BEs) of 458.2–458.5 and 464.3–464.2 eV, referred to as the spin–orbit splitting of Ti $2p_{3/2}$ and Ti $2p_{1/2}$, respectively. These peaks correlated to the characteristic Ti–O–Ti bond in TiO_2.[17] Compared to those of UT-W and UT-E, the Ti $2p_{3/2}$ peak of UT-M shifted to lower binding energy by 0.3 eV and 0.1 eV, while the Ti $2p_{1/2}$ peak also shifted slightly, suggesting the formation of a small fraction of Ti cations with lower oxidation state in UT-M. The lowering of the Ti 2p binding energy should accompany the presence of O_v in UT-M and the ESR measurement under the dark and N_2 atmospheres revealed that the UT-M sample displayed the strongest signal of the peak with a *g* factor of 2.003,[18] confirming the highest concentration of oxygen defects on its surface. The O 1s XPS spectra are deconvoluted into two peaks assigned to lattice oxygen (labeled as O_L, BE = 530.4 eV) and surface hydroxyl species (labeled as O_H, BE = 532.1 eV) (Fig. 3(b)). The ratio of peak areas of O_H to (O_L + O_H) (%) indicated that more surface hydroxyl species were present on the UT-M surface than on the other two samples. The water contact angle analysis (Fig. S15, ESI†) was consistent with the XPS analysis, which suggested additional hydroxyl groups on the UT-M surface benefiting the generation of liquid products.

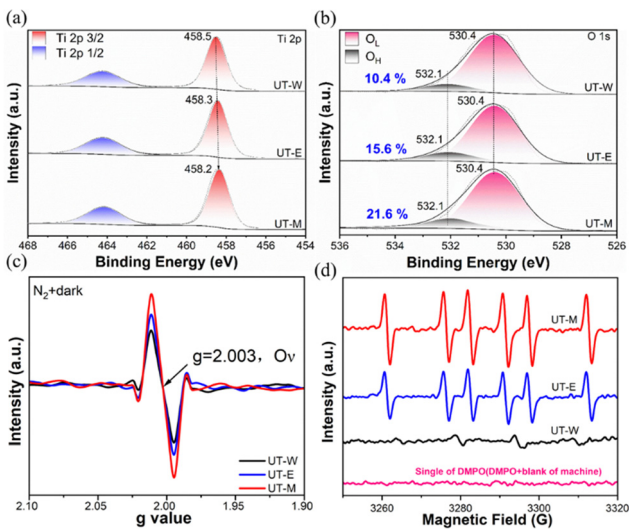

Fig. 3 Surface properties of UT-W, UT-M, and UT-E. (a) Ti 2p and (b) O 1s XPS spectra; (c) EPR spectra of the O vacancy; and (d) *in situ* ESR signal of $^{\bullet}CO_2^-$.

It is worth mentioning that the organic species on the surface of three ultrathin TiO_2 catalysts also played a significant role in the catalytic cycle. As shown by thermogravimetric analysis (TG-DTA) and infrared (IR) spectroscopy results (Fig. S16 and S17, ESI†), abundant ethylene glycolate (EG) radicals (21.6–24.1 wt%) cover the surface of the ultrathin TiO_2 nanosheets, which is advantageous for carbon oxygen hydrogenation.[16] Once exposed to UV, electrons were trapped in Ti-3d orbitals, forming Ti^{3+} sites, and holes broke the Ti–O bonds between glycolate and TiO_2, leading to the formation of $-OCH_2CH_2O^{\bullet}$ radicals (Fig. S18, ESI†). Because of the presence of α-H, $-OCH_2CH_2O^{\bullet}$ was unstable and would undergo hydrogen transfer to give $-OCH_2{\cdot}CHOH$. We also tested UT-M's photocatalytic performance after removing the EG by calcining at different temperatures in air. The results proved that the EG indeed played a role and also showed that only gaseous CO and CH_4 were observed in both the UT-300 and UT-350 samples (Fig. S6 and S19, ESI†). We have already ruled out the possible product formation directly from the EG species, evidenced by the isotopic exchange measurements (Fig. 2(c)). Therefore, it is rationalized that it reduces the recombination rate of the electron–hole pairs and provides more hydroxyl species as a proton source.

CO_2 is chemically inert under ambient conditions, which makes its adsorption and activation steps crucial for the reduction. The CO_2 adsorption measurements suggested that UT-M possesses the highest CO_2 uptake capacity (Fig. S20, ESI†). Additionally, *in situ* CO_2 adsorption diffuse reflectance infrared Fourier transformed spectroscopy (DRIFTS) of the three catalysts suggested that the binding of the CO_2 reactant was more favorable on UT-M (Fig. S21, ESI†). Furthermore, the *in situ* ESR results demonstrated that the UT-M had the highest DMPO-$^{\bullet}CO_2^-$ signal where the $^{\bullet}CO_2^-$ generation was the key step in CO_2 reduction (Fig. 3(d)).

It is clear that the liquid products are all derived from the CO_2 feed instead of the EG radicals. The *in situ* DRIFTS semi-quantitative analysis was further carried out to gain insights into the intermediate species and the underlying reaction mechanism. In the *in situ* DRIFTS spectra of the three samples (Fig. S22, ESI†), the three key intermediate species of *COOH, $*OCH_3$, and *COCO were all detected, verifying the high consistency of the ultrathin structure. To further clarify the possible mechanism, we list in Table S4 (ESI†) the relationship between the product yield of the samples and the IR intensities of the corresponding key intermediates. Take the example of *COCO and the corresponding generated C_2H_5OH. The θ_1, θ_2 and θ_3 of the C_2H_5OH yields are 1.23, 2.22 and 1.81, while the *COCO IR intensities are 1.22, 2.20 and 1.80 (note: θ_1, θ_2 and θ_3 represent the ratio of UT-M to UT-E, the ratio of UT-M to UT-W,

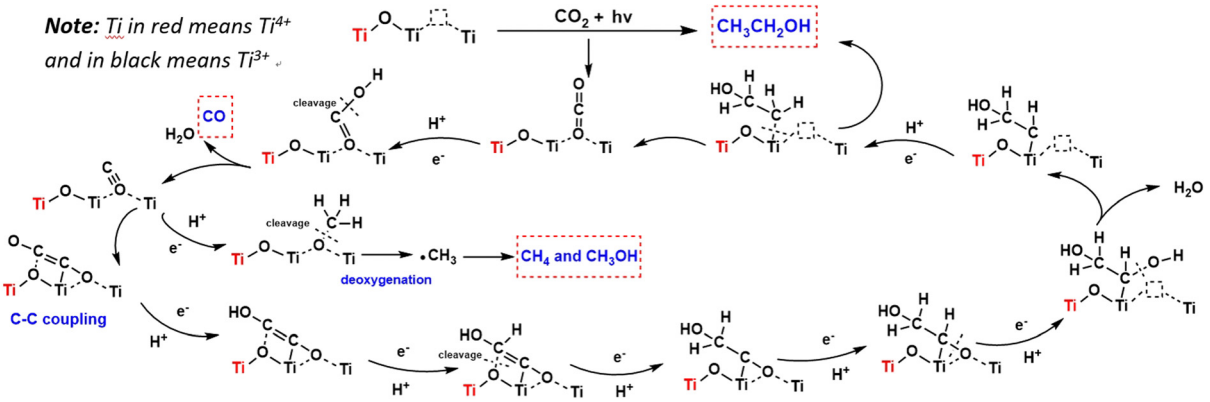

Fig. 4 Proposed mechanism of CO_2 photoreduction over ultrathin TiO_2 nanosheets.

and the ratio of UT-E to UT-W, respectively). Therefore, the semi-quantitative analysis results are good evidence that C_2H_5OH is generated *via* *COCO. Similarly, it is well demonstrated that CH_3OH and CO are derived from $*OCH_3$ and *COOH, respectively. Based on the *in situ* DRIFTS semi-quantitative analysis results, a possible pathway is proposed in Fig. 4. The surface oxygen vacancies and hydroxyl groups act as a proton source and are the key factors for CO_2 reduction. When CO_2 diffuses to O_v, the reaction for the generation of CH_4/CH_3OH would undergo a fast-hydrogenation (FH) path. For the FH path, it is found that surface oxygen vacancies can greatly lower the barrier of the deoxygenation processes, which makes it a more active site than the surface Ti.[19] The details are shown in Fig. S23 and Table S5 (ESI†). When CO_2 was introduced, the O atom in CO_2 adsorbed on the O_v of ultrathin TiO_2 and then the adsorbed CO_2 is reduced to *CO through a *COOH intermediate. The desorption of some minority *CO results in a gaseous CO product, while the majority of *CO undergoes further coupling with another *CO to form *COCO intermediates on O_v–Ti–O_L sites. Afterwards, under the concerted electron–proton transfer, the *COCO subsequently undergoes hydrogenation to form *COCOH. This is followed by a series of cascading hydrogenations from *COCOH to $*CHOHCH_2OH$, which ultimately dehydrates to$*CH_2CH_2OH$. Meanwhile, the *CO could also be hydrogenated to $*OCH_3$, followed by deoxygenation to form $^{\bullet}CH_3$. Whether the CH_3OH or CH_4 is produced depends on several factors, such as the hydrophilicity of the surface and the amount of water in the catalysis.

In summary, significant productivity has been attained for liquid products (up to *ca.* 463.9 μmol g^{-1} in 8 hours). The abundant surface oxygen defects on the ultrathin TiO_2 nanosheets act as CO_2 adsorption and activation sites. Through the O_v–Ti–O_L unit, CO_2 can be selectively coordinated at a favorable reaction center for C–C coupling, thereby facilitating multistep photocatalytic reduction. Furthermore, the appropriate thickness of the TiO_2 nanosheets reduces the charge-transfer resistance and active *C2 intermediates are further hydrogenated to C_2H_5OH with the assistance of hydroxyl protons and electrons. The findings in this study may provide a new idea for designing and synthesizing noble metal-free photocatalysts for the generation of multicarbon fuels powered by light.

This work was supported by State Key Laboratory of Catalytic Materials and Reaction Engineering (RIPP, SINOPEC), the National Natural Science Foundation of China (21976082, 22106067), and funding from China Petroleum & Chemical Corp. (No. 122003).

Conflicts of interest

There are no conflicts to declare.

Notes and references

1 G. Wang, C. T. He, R. Huang, J. Mao, D. Wang and Y. Li, *J. Am. Chem. Soc.*, 2020, **142**, 19339–19345.
2 S. C. Roy, O. K. Varghese, M. Paulose and C. A. Grimes, *ACS Nano*, 2010, **4**, 1259.
3 P. Sharma, S. Kumar, O. Tomanec, M. Petr, J. Zhu Chen, J. T. Miller, R. S. Varma, M. B. Gawande and R. Zboril, *Small*, 2021, **17**, e2006478.
4 J. Fu, K. Jiang, X. Qiu, J. Yu and M. Liu, *Mater. Today*, 2020, **32**, 222–243.
5 T. Zhang, J. C. Bui, Z. Li, A. T. Bell, A. Z. Weber and J. Wu, *Nat. Catal.*, 2022, **5**, 202–211.
6 S. N. Habisreutinger, L. Schmidt-Mende and J. K. Stolarczyk, *Angew. Chem., Int. Ed.*, 2013, **52**, 7372–7408.
7 H. Zhou, M. Wang, F. Kong, Z. Chen, Z. Dou and F. Wang, *J. Am. Chem. Soc.*, 2022, **144**, 21224–21231.
8 W. Li, A. Elzatahry, D. Aldhayan and D. Zhao, *Chem. Soc. Rev.*, 2018, **47**, 8203–8237.
9 Y. Guo, K. Xu, C. Wu, J. Zhao and Y. Xie, *Chem. Soc. Rev.*, 2015, **44**, 637–646.
10 W. Bi, C. Wu and Y. Xie, *ACS Energy Lett.*, 2018, **3**, 624–633.
11 J. Mei, T. Liao, L. Kou and Z. Sun, *Adv. Mater.*, 2017, **29**, 117–127.
12 S. Chen, H. Wang, Z. Kang, S. Jin, X. Zhang, X. Zheng, Z. Qi, J. Zhu, B. Pan and Y. Xie, *Nat. Commun.*, 2019, **10**, 788.
13 B. Huang, M. A. McGuire, A. F. May, D. Xiao, P. Jarillo-Herrero and X. Xu, *Nat. Mater.*, 2020, **19**, 1276–1289.
14 Y. Zhao, G. Chen, T. Bian, C. Zhou, G. I. Waterhouse, L. Z. Wu, C. H. Tung, L. J. Smith, D. O'Hare and T. Zhang, *Adv. Mater.*, 2015, **27**, 7824–7831.
15 G. Xiang, T. Li, J. Zhuang and X. Wang, *Chem. Commun.*, 2010, **46**, 6801–6803.
16 P. Liu, Y. Zhao, R. Qin, S. Mo, G. Chen, L. Gu, D. Chevrier, P. Zhang, Q. Guo, D. Zang, B. Wu, G. Fu and N. Zheng, *Science*, 2016, **352**, 797–800.
17 B. Wang, X. Li, S. Liang, R. Chu, D. Zhang, H. Chen, M. Wang, S. Zhou, W. Chen, X. Cao and W. Feng, *Phys. Chem. Chem. Phys.*, 2020, **22**, 9943–9953.
18 J. Li, M. Zhang, Z. Guan, Q. Li, C. He and J. Yang, *Appl. Catal., B*, 2017, **206**, 300–307.
19 Y. Ji and Y. Luo, *J. Am. Chem. Soc.*, 2016, **138**, 15896–15902.

